Geophysical Prospecting EAGE EUROPEAN ASSOCIATION OF GEOSCIENTISTS & ENGINEERS

Geophysical Prospecting, 2013, **61**, 75–91 doi: 10.1111/j.1365-2478.2012.01024.x

Wide-azimuth angle gathers for anisotropic wave-equation migration

Paul Sava[1*] and Tariq Alkhalifah[2]

[1]*Center for Wave Phenomena, Colorado School of Mines, and* [2]*King Abdullah University of Science and Technology*

Received June 2011, revision accepted October 2011

ABSTRACT

Extended common-image-point gathers (CIP) constructed by wide-azimuth TI wave-equation migration contain all the necessary information for angle decomposition as a function of the reflection and azimuth angles at selected locations in the subsurface. The aperture and azimuth angles are derived from the extended images using analytic relations between the space- and time-lag extensions using information which is already available at the time of migration, i.e. the anisotropic model parameters. CIPs are cheap to compute because they can be distributed in the image at the most relevant positions, as indicated by the geologic structure. If the reflector dip is known at the CIP locations, then the computational cost can be reduced by evaluating only two components of the space-lag vector. The transformation from extended images to angle gathers is a planar Radon transform which depends on the local medium parameters. This transformation allows us to separate all illumination directions for a given experiment, or between different experiments. We do not need to decompose the reconstructed wavefields or to choose the most energetic directions for decomposition. Applications of the method include illumination studies in complex areas where ray-based methods fail, and assuming that the subsurface illumination is sufficiently dense, the study of amplitude variation with aperture and azimuth angles.

Key words: Wave-equation, Migration, Angle gathers, Anisotropy.

INTRODUCTION

Wave-equation depth migration is a powerful tool for accurately imaging complex geology. Imaging accuracy depends on the quality of the earth model and on the technique used for wavefield reconstruction (Gray et al., 2001). This is particularly true for imaging in areas characterized both by strong anisotropy, as well as complex heterogeneous geology. Such challenges can best be addressed by imaging using reverse-time migration (Baysal et al., 1983; McMechan, 1983), a computationally intensive method, but capable of providing the most accurate representation of complex geologic structure.

Angle domain imaging complements conventional structural imaging by indicating the subsurface illumination patterns. This method could also potentially be used for velocity verification and estimation and amplitude variation with angle analysis, which could lead to accurate geologic interpretation. Angle decomposition methods can be classified based on the technique used to simulate wave propagation in the subsurface as ray methods (Xu et al., 1998; Brandsberg-Dahl et al., 2003) or wavefield methods (de Bruin, Wapenaar, and Berkhout, 1990; Xie and Wu, 2002; Sava and Fomel, 2003; Biondi and Symes, 2004; Wu and Chen, 2006; Xu, Zhang, and Tang, 2010; Sava and Vlad, 2011). In principle, the gathers produced by these different methods have similar uses since they characterize the reflectivity variation with the incidence and azimuth angles. However, the wavefield methods are superior because they describe more accurately wave propagation in complex geologic structures. The wavefield methods can be differentiated by the domain in which they are applied, i.e. before or after the imaging condition. The methods

* E-mail: psava@mines.edu

© 2012 European Association of Geoscientists & Engineers

operating before the imaging condition decompose the extrapolated wavefields directly (de Bruin et al., 1990; Wu and Chen, 2006; Xu et al., 2010), which makes this technique costly since it operates on large wavefields characterized by complex multipathing. In contrast, the methods applied after the imaging condition decompose the images which are represented as a function of space and parameters referred to as extensions (Rickett and Sava, 2002; Sava and Fomel, 2006; Sava and Vasconcelos, 2011). In both cases we obtain angle-dependent reflectivity in the form of the scattering matrix (Wu and Chen, 2006), although the cost associated with the decomposition is significantly different.

Angle-domain imaging is often based on common-image-gathers (CIGs) which represent the reflectivity as a function of reflection angles and a space axis, e.g. the depth axis. In this paper, we focus on angle decomposition using extended common-image-point-gathers (CIPs), which offer significant computational savings over alternative methods based on CIGs. For a complete discussion of the merits of using common-image-point gathers we refer to Sava and Vasconcelos (2011).

Wave-equation angle-domain imaging of wide-azimuth data (Regone, 2006; Michell et al., 2006; Clarke et al., 2006) is particularly challenging due to the larger data volume and the difficulty of interpreting multi-dimensional data. Wide-azimuth angle decomposition can be done using ray methods (Koren et al., 2008) or with wavefield methods applied before the imaging condition (Zhu and Wu, 2010; Biondi and Tisserant, 2004; Xu et al., 2010) or after the imaging condition (Sava and Fomel, 2005; Sava and Vlad, 2011). Here, we focus on imaging with wavefield methods which are more accurate and robust in complex geology.

Typical Earth layering leads to wave propagation that can be best described using anisotropic media, specifically transversely isotropic (TI). Anisotropy describes media with wave speed changing with the propagation angle, thus making angle gathers a natural domain for anisotropic velocity analysis. Alkhalifah and Fomel (2010) derive analytical relations to construct angle gathers for TI media with a vertical symmetry axis (VTI) from downward continued wavefields prior to the application of an imaging condition. This approach requires wavefields in the wavenumber domain, and thus, it is generally limited to downward continuation methods. Similarly, Alkhalifah and Sava (2010) provide a framework to construct angle gathers for dip-constrained TI media (DTI). This model allows for an analytical description of the angle gather mapping process applied prior to the imaging condition, and it is also appropriate for downward continuation imaging methods. In addition, this technique requires media that satisfy the dip constraint.

In this paper, we develop a technique for mapping the image extensions to angle gathers in general TI media with symmetry axis direction oriented arbitrarily in a 3D space. We focus on imaging methods using time-domain wavefield extrapolation, i.e. reverse-time migration. Our technique utilizes indirectly local plane wave decompositions of extended images and exploits information about the anisotropy characterizing the imaged medium. We show that this formulation produces an accurate description of the specular reflection for general 3D TI media, at an affordable cost for large wide-azimuth data.

WAVE-EQUATION IMAGING

Conventional seismic imaging uses the concept of single scattering: waves propagate from seismic sources, interact with discontinuities and return to the surface as reflected seismic waves. The "source" and "receiver" wavefields associated with the propagation from the sources to the reflectors and with the propagation from the reflectors to the receivers coincide kinematically on the reflectors (Berkhout, 1982; Clærbout, 1985). Wavefield-based imaging consists of wavefield reconstruction and the imaging condition. The key elements are the source and receiver wavefields, W_s and W_r which are 4-dimensional objects as a function of space $\mathbf{x} = \{x, y, z\}$ and time t (or, equivalently, frequency ω). During wavefield reconstruction, we solve numerically a wave equation using the recorded data as boundary and initial conditions. Then, in the imaging condition we identify the subsurface locations where the reconstructed wavefields match kinematically in time.

Wavefield reconstruction in tilted TI anisotropic media, requires a numeric solutions to a pseudo-acoustic wave-equation. Different pseudo-acoustic wave-equations are reported in the literature, their main differences being in the order of the equation and the implementation used. The method discussed in this paper does not depend on any specific implementation. Our choice is to use the time-domain method of Fletcher et al. (2009) and Fowler et al. (2010) which consists of solving a system of second-order coupled equations:

$$\frac{\partial^2 p}{\partial t^2} = v_{p_x}^2 H_2[p] + v_{p_z}^2 H_1[q] \,, \tag{1}$$

$$\frac{\partial^2 q}{\partial t^2} = v_{p_n}^2 H_2[p] + v_{p_z}^2 H_1[q] \,. \tag{2}$$

Here, p and q are two wavefields depending on space $\mathbf{x} = \{x, y, z\}$ and time t coordinates. H_1 and H_2 are differential

operators applied to the quantity in the square brackets. The velocities v_{p_z}, v_{p_x}, and v_{p_n} are the vertical, horizontal and "NMO" velocities used to parametrize a generic TTI medium. These expressions assume that the shear-wave velocity (v_{s_z}) is zero, which leads to well-known wavefield artifacts (Alkhalifah, 2000) visible in our numeric examples. These artifacts are heavily distorted shear waves due to the approximation made on their propagation velocity. An alternative implementation of equations 1-2 allow for non-zero shear-wave velocity which reduces the strength of the artifacts. We do not emphasize this choice here, since it does not affect our angle decomposition method. We concentrate on angle-domain imaging with the quasi-P wave mode which is accurately described, although the extrapolation with these relations shows instability in general TTI media. Alternative formulations, e.g. Duveneck and Bakker (2011) and Zhang et al. (2011) provide expressions for stable extrapolation in more general cases, including TTI. We do not elaborate further on the different methods for pseudo-acoustic extrapolation because our method is independent of the extrapolation technique.

If we describe the medium using the parameters introduced by Thomsen (2001), the velocities are related to the anisotropy parameters ϵ and δ by the relations

$$v_{p_n} = v_{p_z}\sqrt{1+2\delta}, \tag{3}$$

$$v_{p_x} = v_{p_z}\sqrt{1+2\epsilon}. \tag{4}$$

Thus, the quantities H_1 and H_2 are defined as

$$\begin{aligned} H_1 = {} & \sin^2\theta_a\cos^2\phi_a\frac{\partial^2}{\partial x^2} + \sin^2\theta_a\sin^2\phi_a\frac{\partial^2}{\partial y^2} + \cos^2\theta_a\frac{\partial^2}{\partial z^2} \\ & + \sin^2\theta_a\sin 2\phi_a\frac{\partial^2}{\partial x\partial y} + \sin 2\theta_a\sin^2\phi_a\frac{\partial^2}{\partial y\partial z} \\ & + \sin 2\theta_a\cos\phi_a\frac{\partial^2}{\partial z\partial x}, \end{aligned} \tag{5}$$

$$H_2 = \frac{\partial^2}{\partial x^2} + \frac{\partial^2}{\partial y^2} + \frac{\partial^2}{\partial z^2} - H_1, \tag{6}$$

where θ_a describes the angle made by the TI symmetry axis with the vertical and ϕ_a the azimuth angle of the plane that contains the tilt direction. In this paper, we assume that all parameters characterizing the TI medium are known, including the angles θ_a and ϕ_a. Therefore, we can use this procedure to reconstruct wavefields with arbitrary heterogeneity, including that of the anisotropy and tilt parameters. Here, we do not make any assumption about the orientation of the tilt medium, i.e. the tilt axis does not have to be aligned with the normal of the reflector at any point in the image.

A conventional imaging condition based on the reconstructed wavefields defines the image as the zero lag of the cross-correlation between the source and receiver wavefields (Clærbout, 1985):

$$R(\mathbf{x}) = \sum_{shots}\sum_{t} W_s(\mathbf{x},t)\, W_r(\mathbf{x},t), \tag{7}$$

where R represents the migrated image which depends on position $\mathbf{x}$. An extended imaging condition is a generalization of the conventional imaging condition in that it retains in the output image acquisition or illumination parameters. Since in shot record migration the source and receiver wavefields are reconstructed on the same computational grid, there is no a-priori wavefield separation that can be retained in the output image. In this case, we can generate the extensions by correlation of the wavefields shifted symmetrically in space (Rickett and Sava, 2002; Sava and Fomel, 2005) or in time Sava and Fomel (2006). This separation is simply the lag of the cross-correlation between the source and receiver wavefields (Sava and Vasconcelos, 2011):

$$R(\mathbf{x},\boldsymbol{\lambda},\tau) = \sum_{shots}\sum_{t} W_s(\mathbf{x}-\boldsymbol{\lambda},t-\tau)\, W_r(\mathbf{x}+\boldsymbol{\lambda},t+\tau). \tag{8}$$

The quantities $\boldsymbol{\lambda}$ and τ are cross-correlation lags in space and time, respectively. Equation 7 represents a special case of equation 8 for $\boldsymbol{\lambda}=0$ and $\tau=0$. Equivalent equations can be written for imaging in the frequency domain (Sava and Vasconcelos, 2011). Various techniques have been proposed to convert the space- and time-lag extensions into reflection angles (Sava and Fomel, 2003, 2006; Sava and Vlad, 2011), thus facilitating amplitude and velocity analysis in complex geologic structures.

In this paper, we use extended common-image-point-gathers to extract angle-dependent reflectivity at individual points in the image. The method described in the following section is appropriate for 3D anisotropic wide-azimuth wave-equation imaging and is analogous to the procedure outlined by Sava and Vlad (2011) for isotropic media. The problem we are solving is to decompose extended CIPs as a function of azimuth ϕ and reflection θ angles at selected points in the image:

$$R(\boldsymbol{\lambda},\tau) \Longrightarrow R(\phi,\theta,\tau). \tag{9}$$

However, we assume that all parmeters characterizing the anisotropic medium are known. Therefore, all the energy in the output CIPs concentrates at $\tau=0$, so we can focus on the particular case of decomposition which does not preserve the time-lag variable in the output: $R(\boldsymbol{\lambda},\tau) \Longrightarrow R(\phi,\theta)$. The topic of angle decomposition when the gathers are constructed with

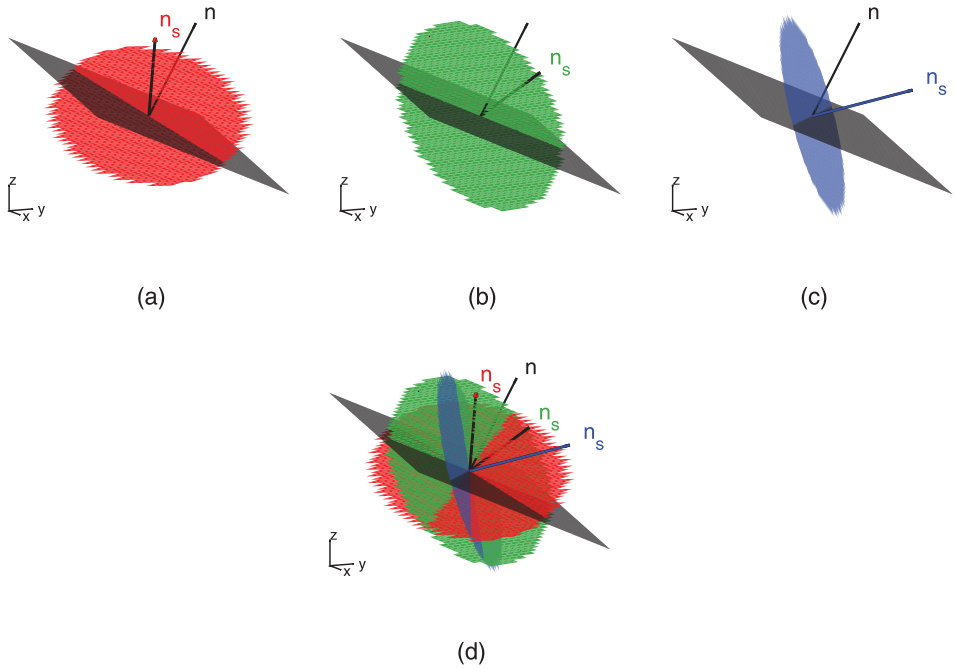


Figure 1. Schematic representation of three planes representing independent branches of a wavefield at their interaction with a reflector. Panels (a)-(c) show the individual wavefield branches separated by propagation direction, and panel (d) shows their superposition. The extended imaging condition uses the wavefields as in panel (d), but for the purpose of angle decomposition we can study the individual components.

an incorrect model remains outside the scope of this paper, although the general ideas used here remain valid. We emphasize that the CIPs are constructed only at a small set of points selected along the most relevant image features. This operation can be done automatically, for example by the technique described by Cullison and Sava (2011).

In the remainder of the paper, we derive the moveout function for extended images and develop of procedure for angle decomposition applicable to arbitrary TTI media. We illustrate the procedure with 3D wide-azimuth synthetic examples.

MOVEOUT ANALYSIS

Angle decomposition methods often make the assumption that we can describe reflections using locally planar objects. It is typically assumed that (locally) the reflector is a plane, and that the incident and reflected wavefields are also (locally) planar, thus we can define vectors in-between which we measure incidence and reflection angles and the azimuth of the reflection plane. We formulate our method under this assumption, but do not assume that the wavefronts are planar. We describe each (complex) wavefront as a superposition of planes with different orientations and analyze how each individual plane is used by the extended imaging condition before angle decomposition.

In general, we can distinguish two situations illustrated by Figures 1(a)-1(d).

- First, if the wavefields (source or receiver) correspond to unique propagation paths but are non-planar, we can decompose them in planar components. Using rays, this is analogous to saying that we discuss one pair of incident and reflected rays at an image point.
- Second, if the wavefields (source or receiver) correspond to multiple propagation paths, then we need to consider all (planar) components corresponding to the various branches of the wavefield. Using rays, this is analogous to saying that we discuss all pairs of incident and reflected rays at a given point.

In general, the wavefields may be characterized by a superposition of the two phenomena discussed here.

In our procedure, we do not explicitly decompose the wavefields in planar components corresponding to different branches of the wavefield. Instead, we discuss how each one of these planes behaves during the extended imaging and angle decomposition. We can consider the entire wavefield as a superposition of planes corresponding to the various propagation directions. By linearity, each pair of source and receiver

planes has an expression in the extended images, thus allowing us to decouple different propagation directions after imaging. For example, for the case depicted in Figure 1(d), showing three independent propagation branches, we would obtain three different overlapping but distinct events in the extended image. Thus, we can obtain a map of reflectivity as a function of angles by decomposition of the extended images, regardless of the number of shots which contribute to it or the number of branches that characterize each wavefield at an image point. This approach is cheap relative to procedures that decompose the seismic wavefields explicitly, and we also do not require complicated selections of specific wavefield components identified by their direction of propagation.

For each planar components of the source and receiver wavefields, we can write a geometric equivalent of the conventional imaging condition 7 as

$$\hat{\mathbf{n}}_s \cdot (\mathbf{x} - \mathbf{x}_s) = v_s\,(t - t_s)\,, \tag{10}$$

$$\hat{\mathbf{n}}_r \cdot (\mathbf{x} - \mathbf{x}_r) = v_r\,(t - t_r)\,, \tag{11}$$

where $v_s(\theta, \phi)$ and $v_r(\theta, \phi)$ are velocities characterizing the source and receiver wavefields. In anisotropic media, these velocities depend on the reflection angles θ and ϕ and represent local averages in the space defined by the space lags. The vectors $\hat{\mathbf{n}}_s$ and $\hat{\mathbf{n}}_r$ define the orientation of the source and receiver wavefronts in space, and the quantities $\mathbf{x}_s$, $\mathbf{x}_r$ and t_s, t_r identify the actual position of the wavefront in space and time, respectively, relative to a preset coordinate system (Figure 2). The system 10-11 indicates that the source and receiver wavefields are coincident in space at a given time. In anisotropic media, the velocities for the source and receiver wavefronts depend on the propagation direction. For the case of PP reflections in isotropic media, or in TTI media with an axis of symmetry parallel to the reflector normal, we have $v_s = v_r$. However, for the case when the axis of symmetry is tilted relative to the reflector normal, we have that $v_s \neq v_r$. Here we consider the general case when the two velocities are not equal.

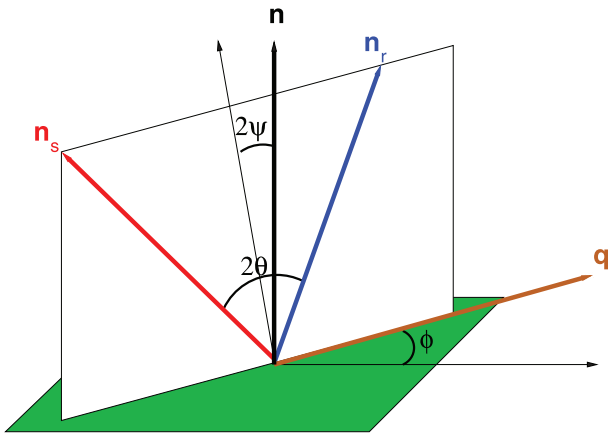


Figure 2. Schematic representation of the vectors used in the derivation of the anisotropic moveout function 33.

Similarly, we can write a geometric equivalent of the extended imaging condition 8 as

$$\hat{\mathbf{n}}_s \cdot (\mathbf{x} - \mathbf{x}_s - \boldsymbol{\lambda}) = v_s\,(t - t_s - \tau)\,, \tag{12}$$

$$\hat{\mathbf{n}}_r \cdot (\mathbf{x} - \mathbf{x}_r + \boldsymbol{\lambda}) = v_r\,(t - t_r + \tau)\,, \tag{13}$$

where $\boldsymbol{\lambda}$ and τ are lags in space and time. The delay is relative to the position and time identified by the conventional imaging condition, equations 10-11. Substituting equation 10 in 12 and 11 in 13, we obtain the expressions

$$\hat{\mathbf{n}}_s \cdot \boldsymbol{\lambda} = v_s \tau, \tag{14}$$

$$\hat{\mathbf{n}}_r \cdot \boldsymbol{\lambda} = v_r \tau\,. \tag{15}$$

We can then replace the vectors $\hat{\mathbf{n}}_s$ and $\hat{\mathbf{n}}_r$ as a function of the normal vector $\hat{\mathbf{n}}$ and the vector $\hat{\mathbf{q}}$ at the intersection of the reflection and the reflector planes (Figure 3)

$$\hat{\mathbf{n}}_s = \hat{\mathbf{q}} \sin\theta_s - \hat{\mathbf{n}} \cos\theta_s, \tag{16}$$

$$\hat{\mathbf{n}}_r = \hat{\mathbf{q}} \sin\theta_r + \hat{\mathbf{n}} \cos\theta_r, \tag{17}$$

where θ_s and θ_r are the (phase) angles made by the source and receiver wavefronts with the normal direction. Therefore, the expressions 14 and 15 become

$$(\hat{\mathbf{q}} \cdot \boldsymbol{\lambda}) \sin\theta_s - (\hat{\mathbf{n}} \cdot \boldsymbol{\lambda}) \cos\theta_s = v_s \tau\,, \tag{18}$$

$$(\hat{\mathbf{q}} \cdot \boldsymbol{\lambda}) \sin\mathtt{tr} + (\hat{\mathbf{n}} \cdot \boldsymbol{\lambda}) \cos\theta_r = v_r \tau. \tag{19}$$

We can separate the quantity $(\hat{\mathbf{q}} \cdot \boldsymbol{\lambda})$ from equations 18 and 19 by multiplying them with $\cos\theta_r$ and $\cos\theta_s$, respectively, followed by summation:

$$(\hat{\mathbf{q}} \cdot \boldsymbol{\lambda})\,[\sin\theta_s \cos\theta_r + \sin\theta_r\ \cos\theta_s] = [v_s \cos\theta_r\ + v_r \cos\theta_s]\tau\,. \tag{20}$$

Likewise, we can separate the quantity $(\hat{\mathbf{n}} \cdot \boldsymbol{\lambda})$ from equations 18 and 19 by multiplying them with $-\sin\theta_r$ and $\sin\theta_s$, respectively, followed by summation:

$$(\hat{\mathbf{n}} \cdot \boldsymbol{\lambda})\,[\sin\theta_r\ \cos\theta_s + \cos\theta_r\ \sin\theta_s] = [-v_s \sin\theta_r\ + v_r \sin\theta_s]\tau\,. \tag{21}$$

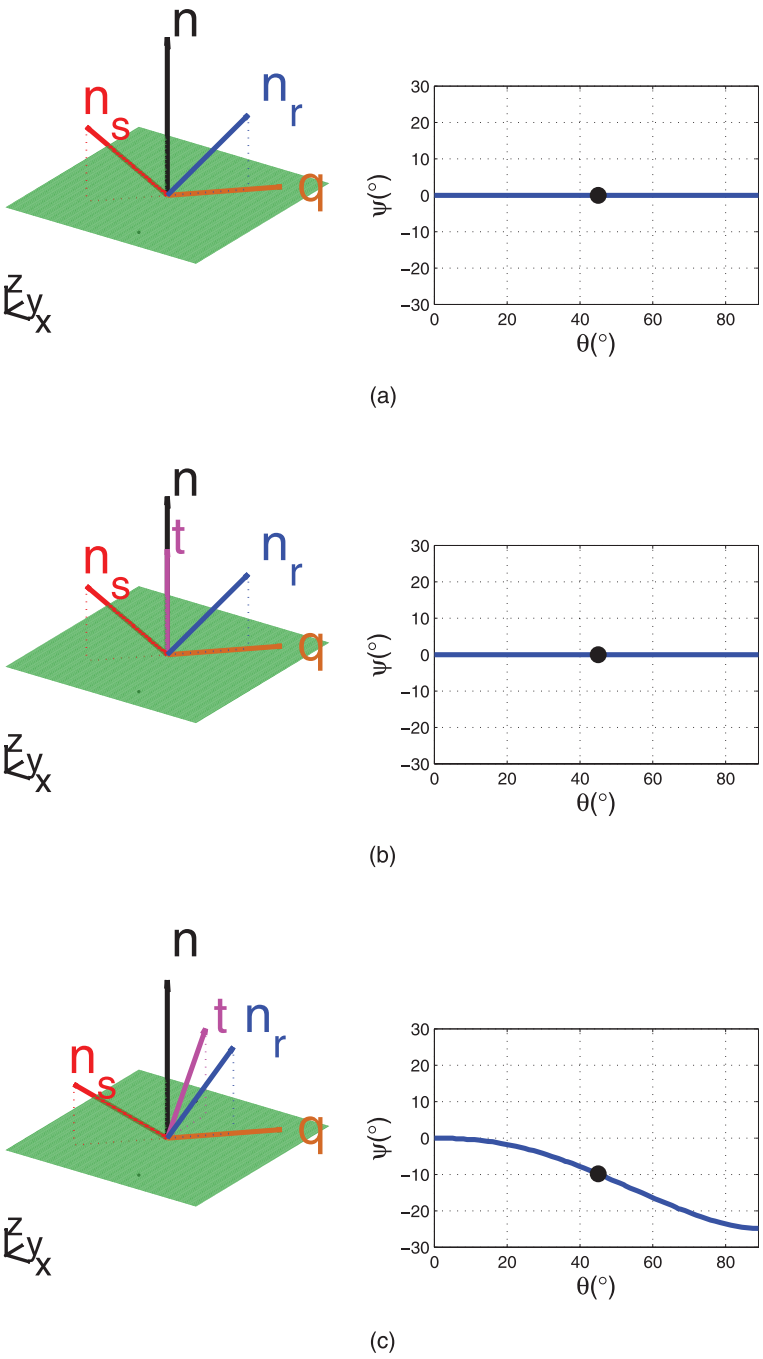


Figure 3. Reflection geometry (left panels) and dependence of the angle ψ with the aperture angle θ (right panels). From top to bottom, the figures correspond to (a) isotropic, (b) VTI and (c) TTI materials.

Using Snell's law

$$\frac{\sin\theta_s}{v_s} = \frac{\sin\theta_r}{v_r}\,, \tag{22}$$

which is valid for any type of media, including the TTI medium considered here, we have

$$v_r \sin\theta_s - v_s \sin\theta_r \;= 0\,. \tag{23}$$

Therefore, after substitution in equations 20 and 21 we can write

$$(\hat{\mathbf{q}}\cdot\boldsymbol{\lambda})\sin(\theta_s+\theta_r) = [v_s\cos\theta_r \;+ v_r\cos\theta_s]\tau, \tag{24}$$

$$(\hat{\mathbf{n}}\cdot\boldsymbol{\lambda})\sin(\theta_s+\theta_r) = 0. \tag{25}$$

The calculations simplify and become more symmetric if we make the notation

$$2\theta = \theta_r + \theta_s \ , \tag{26}$$

$$2\psi = \theta_r - \theta_s, \tag{27}$$

which is equivalent with

$$\theta_s = \theta - \psi, \tag{28}$$

$$\theta_r = \theta + \psi. \tag{29}$$

The angle 2θ represents the sum of the reflection angles on the source and receiver sides, and the angle 2ψ represents their difference. If we label γ the ratio of the velocities on the source and receiver sides, we have

$$\gamma = \frac{v_s}{v_r} = \frac{\sin\theta_s}{\sin\theta_r}, \tag{30}$$

so we can write

$$\gamma = \frac{\sin(\theta - \psi)}{\sin(\theta + \psi)}, \tag{31}$$

or

$$\tan\psi = \frac{1-\gamma}{1+\gamma}\tan\theta. \tag{32}$$

This expression gives us a direct link between the angles θ and ψ. For isotropic or DTI media, we have that $\gamma = 1$, therefore $\tan\psi = 0$ regardless of the angles of incidence or reflection, θ_s and θ_r. Otherwise, the angle ψ depends on the opening angle θ and on the material properties at the reflection point, i.e. the velocities v_s and v_r. On the other hand, the velocities v_s and v_r depend on the angles θ and ψ, thus leading to a circular dependency which we discuss in detail in the following section.

Except for the case of normal incidence ($\theta_s = \theta_r = \theta = 0$ when $\psi = 0$), we can write the system 24-25 as

$$(\hat{\mathbf{q}}\cdot\boldsymbol{\lambda})\sin(2\theta) = [v_s\cos(\theta+\psi) + v_r\cos(\theta-\psi)]\tau \ , \tag{33}$$

$$(\hat{\mathbf{n}}\cdot\boldsymbol{\lambda}) = 0 \ . \tag{34}$$

The system 33-34 characterizes the moveout of PP reflections in a TTI medium with arbitrary symmetry axis direction. We can use this system for wide-azimuth angle decomposition in arbitrary TTI media with a procedure similar to the one outlined in Sava and Vlad (2011) for isotropic media when the system reduces to

$$(\hat{\mathbf{q}}\cdot\boldsymbol{\lambda})\sin\theta = v\tau, \tag{35}$$

$$(\hat{\mathbf{n}}\cdot\boldsymbol{\lambda}) = 0. \tag{36}$$

However, for arbitrary TTI media, the angle decomposition procedure is complicated by the fact that the velocities on the source and receiver sides depend on the angles of incidence. On the other hand, the angles of incidence depend on the velocities, thus leading to a circular dependency. This difficulty can be solved through numeric techniques, as discussed in the following section.

ANGLE DECOMPOSITION

The moveout function derived in the preceding section allows us to assemble an algorithm for wide-azimuth angle decomposition applicable to anisotropic media with arbitrary tilt relative to the reflector. We describe the anisotropic medium by the vertical velocity, v_{p_z}, by the anisotropic parameters ϵ and δ (Thomsen, 2001), and by the tilt vector $\hat{\mathbf{t}}$ which can take an arbitrary orientation relative to the normal vector $\hat{\mathbf{n}}$. This description characterizes the most general case of TTI medium. The DTI case (Alkhalifah and Sava, 2010) is simply a special case for which $\hat{\mathbf{t}} = \hat{\mathbf{n}}$. The vectors $\hat{\mathbf{t}}$ and $\hat{\mathbf{n}}$ are normalized, i.e. $|\hat{\mathbf{t}}| = |\hat{\mathbf{n}}| = 1$.

Isotropic media

As shown in Algorithm 1, at every CIP location we use the information about the known normal vector $\hat{\mathbf{n}}$, measured from the image, and the azimuth reference vector $\hat{\mathbf{v}}$ to compute a reference in the reflection plane, $\hat{\mathbf{a}}$ and extract the velocity v from the model used for migration. As pointed out by Sava and Vlad (2011), the azimuth reference vector $\hat{\mathbf{v}}$ is arbitrary but common for all CIPs, thus allowing us to compare angle-dependent reflectivity at various points in the image. Furthermore, the normal vector allows us to avoid computing one component of the space lag vector, thus significantly reducing the computational cost of the method.

Then, as we loop over all possible values of the azimuth angle ϕ, we construct the vector $\hat{\mathbf{q}}$ at the intersection of the reflector and the reflection planes, Figure 3(a). This operation simply requires a rotation of the azimuth reference vector $\hat{\mathbf{a}}$ around the normal vector $\hat{\mathbf{n}}$ by angle ϕ

$$\hat{\mathbf{q}} = Q(\hat{\mathbf{n}}, \phi)\,\hat{\mathbf{a}} \ , \tag{37}$$

where Q is a rotation matrix defined by the axis $\hat{\mathbf{n}}$ and the angle ϕ. We continue by looping over all possible values of the reflection angle θ and apply a slant-stack to the CIP cube $R(\boldsymbol{\lambda}, \tau)$ using equations 35 and 36. This operation produces the values of the reflectivity for angles θ and ϕ. No wavefield decomposition prior to the imaging condition is required, and

Algorithm 1. Isotropic angle decomposition

```
1:  for each CIP do
2:    input R(λ, τ)
3:    input n̂, v
4:    {n̂, v̂} → â
5:    for φ = 0°...360° do
6:      {n̂, â, φ} → q̂
7:      for θ = 0°...90° do
8:        R(λ, τ) --q̂,θ,v--> R(φ, θ)
9:      end for
10:   end for
11:   return R(φ, θ)
12: end for
```

no wavefield windowing is necessary to select specific wavefield components.

Anisotropic media

The wide-azimuth angle decomposition for anisotropic media follows the same general structure of the isotropic algorithm. As shown in Algorithm 2, at every CIP location, we use the information about the known normal vector $\hat{\mathbf{n}}$, measured from the image, and the azimuth reference vector $\hat{\mathbf{v}}$ to compute a reference in the reflection plane, $\hat{\mathbf{a}}$. We also extract at every location the vertical migration velocity, as well as the anisotropy parameters ϵ and δ, and the tilt vector $\hat{\mathbf{t}}$ describing the TTI medium. All these parameters are known at the time of migration.

Algorithm 2. TTI angle decomposition

```
1:  for each CIP do
2:    input R(λ, τ)
3:    input n̂, v_pz, ε, δ, t̂
4:    {n̂, v̂} → â
5:    for φ = 0° ... 360° do
6:      {n̂, â, φ} → q̂
7:      for θ = 0° ... 90° do
8:        {n̂, q̂, θ, v_pz, ε, δ, t̂} → {v_s, v_r, ψ}
9:        R(λ, τ) --q̂,θ,v_s,v_r,ψ--> R(φ, θ)
10:     end for
11:   end for
12:   return R(φ, θ)
13: end for
```

Then, as for the isotropic algorithm, we loop over all possible values of the azimuth angle ϕ to compute the azimuth vector $\hat{\mathbf{q}}$, and over the reflection angles θ. The next step is the main difference with the isotropic algorithm. Instead of proceeding directly with the slant-stack from the CIP to the angle gather, we first need to evaluate the angle ψ defined in the preceding section. This calculation cannot be done analytically due to the circular dependence between the velocities and phase angles in anisotropic media, but requires a numeric solution. A simple and effective numeric solution is to loop over all possible values of the angle ψ and select the one for which Snell's law is best satisfied. This is cheap calculation which could be done before angle decomposition at the locations where CIPs are constructed. The steps of the algorithm are the following:

1. Evaluate the incidence and reflection angles, θ_s and θ_r.

2. Evaluate the incidence and reflection vectors, $\hat{\mathbf{n}}_s$ and $\hat{\mathbf{n}}_r$, by a simple rotation of the normal vector $\hat{\mathbf{n}}$ with angles θ_s and θ_r around the vector $\hat{\mathbf{b}} = \hat{\mathbf{q}} \times \hat{\mathbf{n}}$.

3. Evaluate the angle α_s and α_r between the incidence and reflection vectors and the tilt vector, $\hat{\mathbf{t}}$.

4. Evaluate the velocities corresponding to angles α_s and α_r relative to the tilt vector using the expression (Tsvankin, 2005)

$$\frac{v^2(\alpha)}{v_{p_z}^2} = 1 + \epsilon \sin^2\alpha - \frac{f}{2}(1-s) \ , \tag{38}$$

where

$$f = 1 - \frac{v_{s_z}^2}{v_{p_z}^2} \ , \tag{39}$$

and

$$s = \sqrt{1 + \frac{4\sin^2\alpha}{f}\left(2\delta\cos^2\alpha - \epsilon\cos 2\alpha\right) + \frac{4\epsilon^2\sin^4\alpha}{f^2}} \ . \tag{40}$$

In our example, we use the acoustic approximation and set $v_{s_z} = 0$. Here α is the angle between the direction of propagation of the source or receiver wavefields, $\hat{\mathbf{n}}_s$ and $\hat{\mathbf{n}}_r$, and the tilt axis $\hat{\mathbf{t}}$, i.e. we are using angles α_s and α_r evaluated in the preceding step.

5. Evaluate the function

$$S(\psi) = v_r \sin\theta_s - v_s \sin\theta_r \ , \tag{41}$$

and decide if the chosen value of ψ minimizes the function $S(\psi)$. The value of ψ that brings the function $S(\psi)$ closest to zero corresponds to the case when Snell's law is observed.

This numeric procedure is summarized in Algorithm 3. Finally, we apply a slant-stack to the CIP cube $R(\boldsymbol{\lambda}, \tau)$ using equations 33 and 34 using the velocities computed before. Thus, we obtain a measure of the reflectivity as a function of the reflection phase angles θ and ϕ.

Algorithm 3. Snell's law in TTI media

get $\{\hat{\mathbf{n}}, \hat{\mathbf{q}}, \theta, v_{p_z}, \epsilon, \delta, \hat{\mathbf{t}}\}$
compute $\{\hat{\mathbf{n}}, \hat{\mathbf{q}}\} \rightarrow \hat{\mathbf{b}}$
$S = huge$
for $\psi^* = \psi_{min} \ldots \psi_{max}$ **do**
  $\theta_s{}^* = \theta - \psi^*$; $\{\hat{\mathbf{b}}, \hat{\mathbf{n}}, \theta_s{}^*\} \rightarrow \hat{\mathbf{n}}_s$; $\{\mathbf{n}_s, \hat{\mathbf{t}}\} \rightarrow \alpha_s$
  Compute $v_s{}^* = v\left(\alpha_s{}^*, v_{p_z}, \epsilon, \delta\right)$
  $\theta_r{}^* = \theta + \psi^*$; $\{\hat{\mathbf{b}}, \hat{\mathbf{n}}, \theta_r{}^*\} \rightarrow \hat{\mathbf{n}}_r$; $\{\mathbf{n}_r, \hat{\mathbf{t}}\} \rightarrow \alpha_r$
  Compute $v_r{}^* = v\left(\alpha_r^*, v_{p_z}, \epsilon, \delta\right)$
  Compute $\{v_s{}^*, \theta_s{}^*, v_r{}^*, \theta_r{}^*\} \rightarrow S^*$
  if$(S^* < S)$ **then**
    $S = S^*$
    $\psi = \psi^*$
    $v_s = v_s{}^*$
    $v_r = v_r{}^*$
  end if
end for
return $\{v_s, v_r, \psi\}$

Figures 3(a)-3(b)-3(c) illustrate the procedure described earlier. In all examples, the left panels depict the vectors characterizing a particular reflection process, i.e. at a given aperture angle 2θ and azimuth $\phi = 45^\circ$, and the right panels depict the dependence of the angle ψ with the reflection angle θ. Figure 3(a) corresponds to reflections in an isotropic material, i.e. $\psi = 0$ for all θ, and Figures 3(b) and 3(c) are for reflections in an anisotropic material characterized by $v_{p_z} = 3.0$ km/s, $\epsilon = 0.45$ and $\delta = -0.29$. In all cases, the normal vector is vertical, i.e. $\hat{\mathbf{n}} = \{0, 0, 1\}$, representing a horizontal reflector. The anisotropic material is VTI, Figure 3(b), or TTI tilted by $\theta_a = 35^\circ$ at azimuth $\phi_a = 90^\circ$ measured from the x axis, Figure 3(c). For the TTI material, the angle ψ is not constant and depends on the material properties, as well as the orientation of the tilt vector and the reflection azimuth. For the special case of DTI materials, i.e. when the normal and anisotropy tilt vectors are aligned, the angle $\psi = 0$. The large dot in the right panels corresponds to the geometry of the vectors shown in the left panels.

EXAMPLES

We illustrate our angle decomposition methodology using three simple examples. The models are homogeneous, with a horizontal reflector, as shown in Figure 4. We consider isotropic, VTI and TTI models characterized by the parameters discussed in the preceding section. Panels 5(a)-5(c)-5(e) show wavefield snapshots, and panels 5(b)-5(d)-5(f) show the data acquired on the surface for the three different cases. As

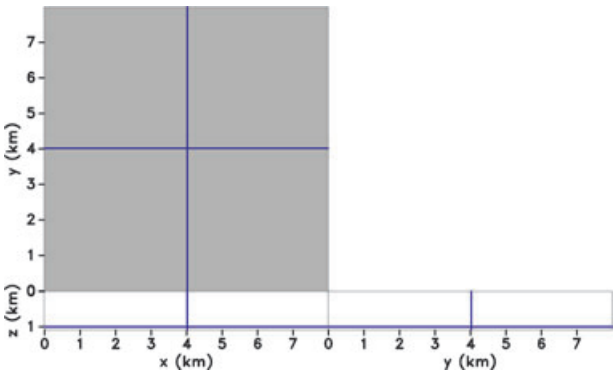


Figure 4. Geometry of the synthetic experiments. The horizontal reflector is located at $z = 1$ km and the sources are distributed on the surface on a regular grid with separation of 0.4 km in x and y.

expected, the moveout observed in the isotropic and VTI cases is azimuthally symmetric, while the moveout observed for the TTI case is not.

Figures 6(a)-6(c)-6(e) show the extended images obtained by reverse-time migration for one shot located on the surface at coordinates $\{x = 4\,\text{km}, y = 4\,\text{km}, z = 0\,\text{km}\}$. The CIP analyzed here is located at $\{x = 4.7\,\text{km}, y = 4.7\,\text{km}, z = 1\,\text{km}\}$. Figures 6(b)-6(d)-6(f) show the corresponding wide-azimuth angle gathers for the extended images in Figures 6(a)-6(c)-6(e), respectively. We use this geometry because the expected reflection and azimuth angles for the homogeneous isotropic medium are $\phi = 45^\circ$ and $\theta = 45^\circ$. Similarly, Figures 7(a)-7(i) show extended CIPs constructed with the TTI data for nine different locations regularly spaced 0.7 km apart on a grid centered on the source located at $\{x = 4\,\text{km}, y = 4\,\text{km}, z = 0\,\text{km}\}$. The extended images are represented along the $\{\lambda_x, \lambda_y, \tau\}$ axes by $\{81, 81, 101\}$ samples in equal increments of $\{0.02$ km, 0.02 km, 0.002 s$\}$.

The dots overlain on the angle-gathers in Figures 6(b)-6(d)-6(f) and Figures 7(a)-7(i) correspond to a numeric estimation of the reflection angles using two-point ray tracing in the given TTI medium. We evaluate the reflection angle θ using the expression (Sava and Fomel, 2006)

$$\tan\theta = \frac{|\mathbf{p}_\text{h}|}{|\mathbf{p}_\text{m}|}, \tag{42}$$

where the quantities $\mathbf{p}_\text{m}$ and $\mathbf{p}_\text{h}$ are evaluated from the source and receiver ray parameters, $\mathbf{p}_\text{s}$ and $\mathbf{p}_\text{r}$, using the expressions

$$\mathbf{p}_\text{m} = \mathbf{p}_\text{r} + \mathbf{p}_\text{s}, \tag{43}$$

$$\mathbf{p}_\text{h} = \mathbf{p}_\text{r} - \mathbf{p}_\text{s}. \tag{44}$$

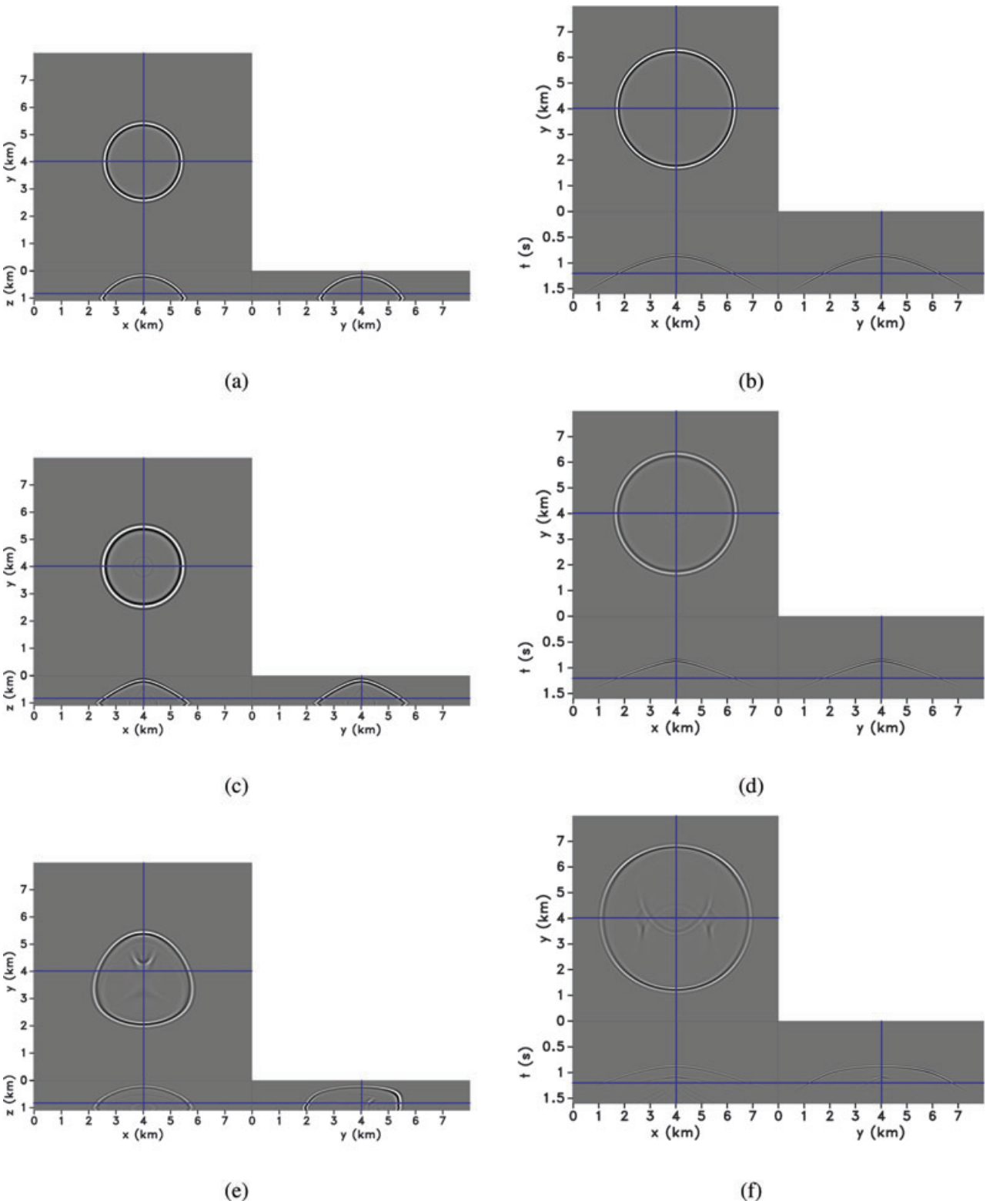


Figure 5. Wavefield snapshots (left panels) and surface data (right panels) for the experiment described in Figure 4. From top to bottom, the panels correspond to (a)-(b) isotropic, (c)-(d) VTI and (e)-(f) TTI materials.

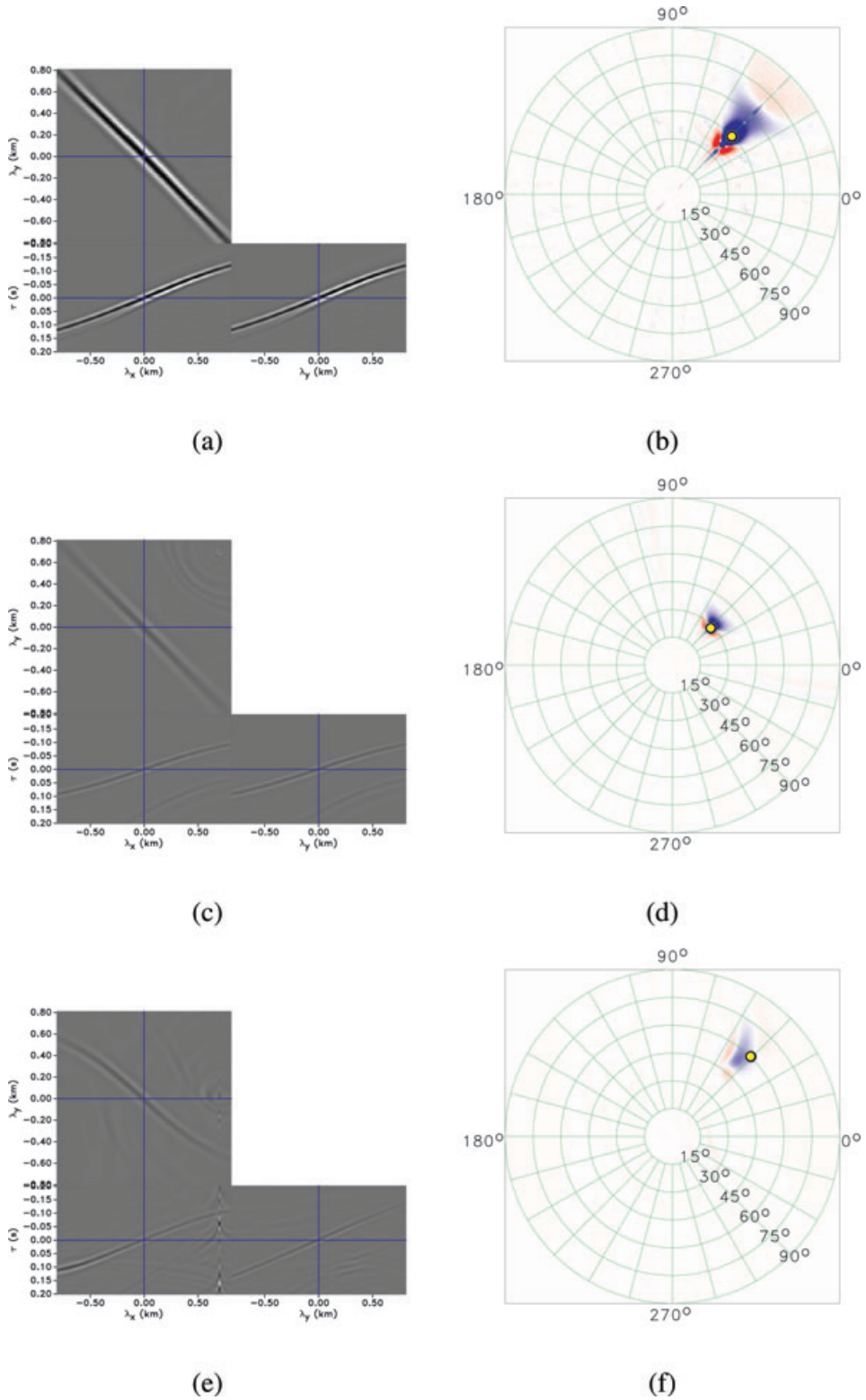


Figure 6. Extended CIPs (left panels) and wide-azimuth angle gathers (right panels) at coordinates $\{x = 4.7\,\text{km}, y = 4.7\,\text{km}, z = 1\,\text{km}\}$ obtained from migration of one source located at $\{x = 4\,\text{km}, y = 4\,\text{km}, z = 0\,\text{km}\}$. From top to bottom, the panels correspond to (a)-(b) isotropic, (c)-(d) VTI and (e)-(f) TTI materials.

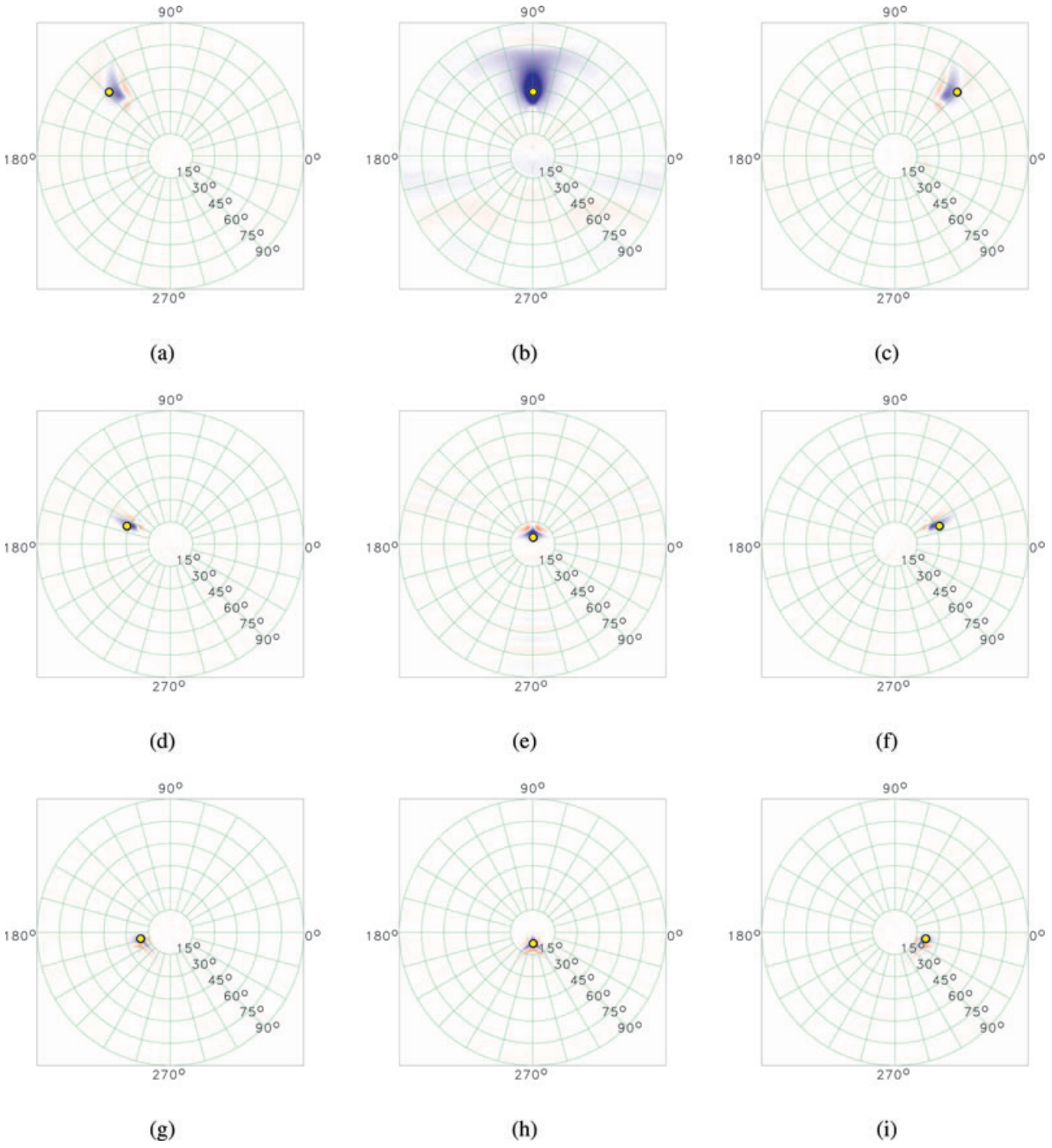


Figure 7. Wide-azimuth angle gathers at nine locations along the reflector distributed in a regular grid with separation of 0.7 km in x and y. The source is at coordinates $\{x = 4\,\text{km}, y = 4\,\text{km}, z = 0\,\text{km}\}$ and the model is characterized by TTI anisotropy.

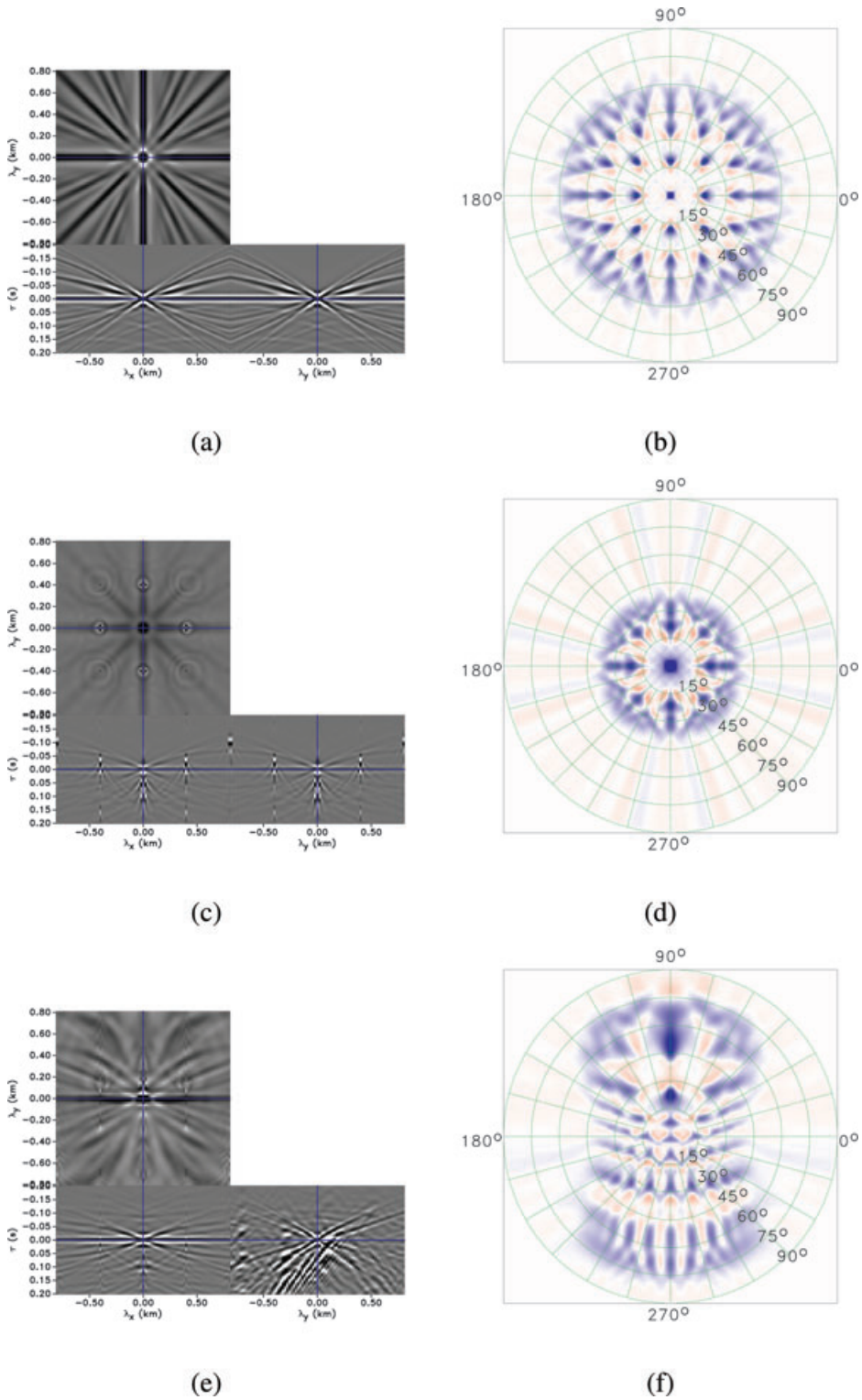


Figure 8. Extended CIPs (left panels) and wide-azimuth angle gathers (right panels) at coordinates $\{x = 4\,\text{km}, y = 4\,\text{km}, z = 1\,\text{km}\}$ obtained from migration of shots located on a regular grid at $z = 0\,\text{km}$ with spacing of 0.4 km in x and y. From top to bottom, the panels correspond to (a)-(b) isotropic, (c)-(d) VTI and (e)-(f) TTI materials.

For a horizontal reflector, the angle ϕ is given by the azimuth of the incident or reflected phase slowness vectors. These examples demonstrate the accuracy of our angle decomposition, even in media characterized by strong anisotropy.

So far, we have demonstrated angle decomposition for independent shots and CIPs, although our technique does not need to be applied to CIPs created independently. Our procedure is capable of separating the expression of different shots from extended CIP. Figures 8(a)-8(f) are similar to Figure 6(a)-6(f), except that imaging is performed using shots located on a regular grid at $z = 0$ km with spacing of 0.4 km in x and y. Each shots illuminates this point in the subsurface at different angles θ and ϕ, as illustrated in Figures 8(b)-8(d)-8(f). When imaging in VTI medium, the reflection angles decrease compared to the isotropic case. When imaging in the TTI medium, the reflection illuminate predominantly in the direction of the tilt, as expected. Each shot leaves a different imprint in the angle-gather.

DISCUSSION

The exploration community is relying increasingly on reverse-time imaging of data from media characterized by transverse isotropy. This imaging method can handle abrupt changes in the symmetry axis direction, as well as heterogeneity in all medium parameters, including velocity and anisotropy. Though the efficiency of the TI reverse-time migration methods leave plenty of room for improvement, our biggest challenge is attaining the anisotropy information required to run these migration algorithms. Building wide-azimuth angle gathers and understanding their dependence on the anisotropy parameters are helpful toward addressing this challenge. The angle gather extraction approach developed here works with reverse-time migration and is specifically designed for processing of wide-azimuth data.

As discussed earlier, angle domain imaging can be done by tracking the wave propagation directions in the reconstructed wavefields at all locations in the subsurface. This is both costly and difficult, since this approach relies on identification of wavepaths in large and complex wavefields, followed by selection of a few most energetic paths for mapping in the angle domain. Our alternative approach uses the intermediate step of constructing the extended images at relevant positions in the subsurface, followed by angle decomposition. All relevant angle-domain information is available in the extended images, which makes the decomposition both cheap and robust, since we do not need to select any specific propagation direction.

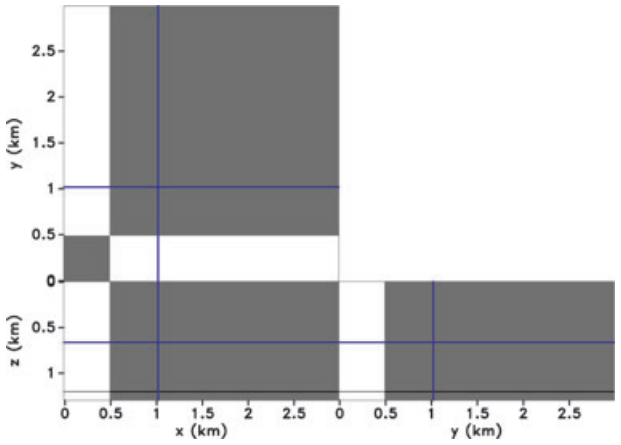


Figure 9. The velocity model for the synthetic experiment showing reflections of triplicating wavefields.

Figures 9-10(b) illustrate this idea. Here, we consider an isotropic model which is generally homogeneous, except for two vertical walls which are arranged to generate additional propagation paths in the center of the model, Figure 9. The source is located at coordinates $\{x = 1\,\text{km}, y = 1\,\text{km}, z = 0\,\text{km}\}$. Figure 10(a) and 10(b) show a wavefield snapshot and the data, respectively, and indicate that there are four different propagation directions causing reflections in the subsurface. Figure 11(a) show the extended CIP at coordinates $\{x = 1\,\text{km}, y = 1\,\text{km}, z = 1.2\,\text{km}\}$. Different reflection paths are visible in the extended cube, but angle decomposition separates these propagation directions as a function of reflection angles. For example, Figure 11(b) shows the corresponding angle gather for the extended CIP shown in Figure 11(a). The four different propagation paths are visible in the image with their respectives amplitude and reflection angles. We can observe a reflection at normal incidence, two reflections at approximately 40° in the 0° and 90° azimuths, and prismatic reflections visible along 45° azimuth. All reflection directions are simultaneously and correctly mapped with no additional cost over the mapping of one individual direction. Furthermore, this conclusion remains true if the extended CIPs are constructed with multiple shots, as seen in the examples presented in the preceding section, or if the wavefield extrapolation is done in TTI media with arbitrary tilt and orientation.

CONCLUSIONS

Wide-azimuth angle decomposition can be performed on individual common-image-point gathers constructed using the extended imaging condition in space and time. The extended

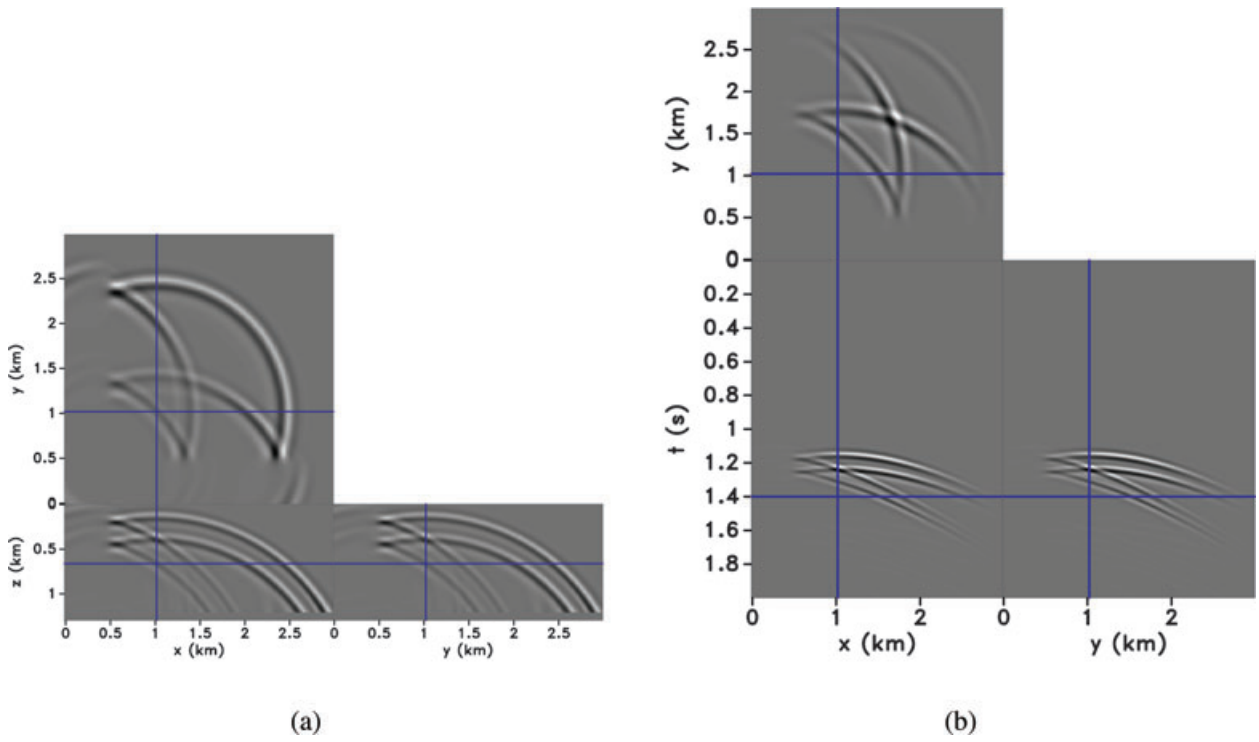


Figure 10. (a) A wavefield snapshot and (b) the data acquired on the surface for the synthetic experiment showing reflections of triplicating wavefields.

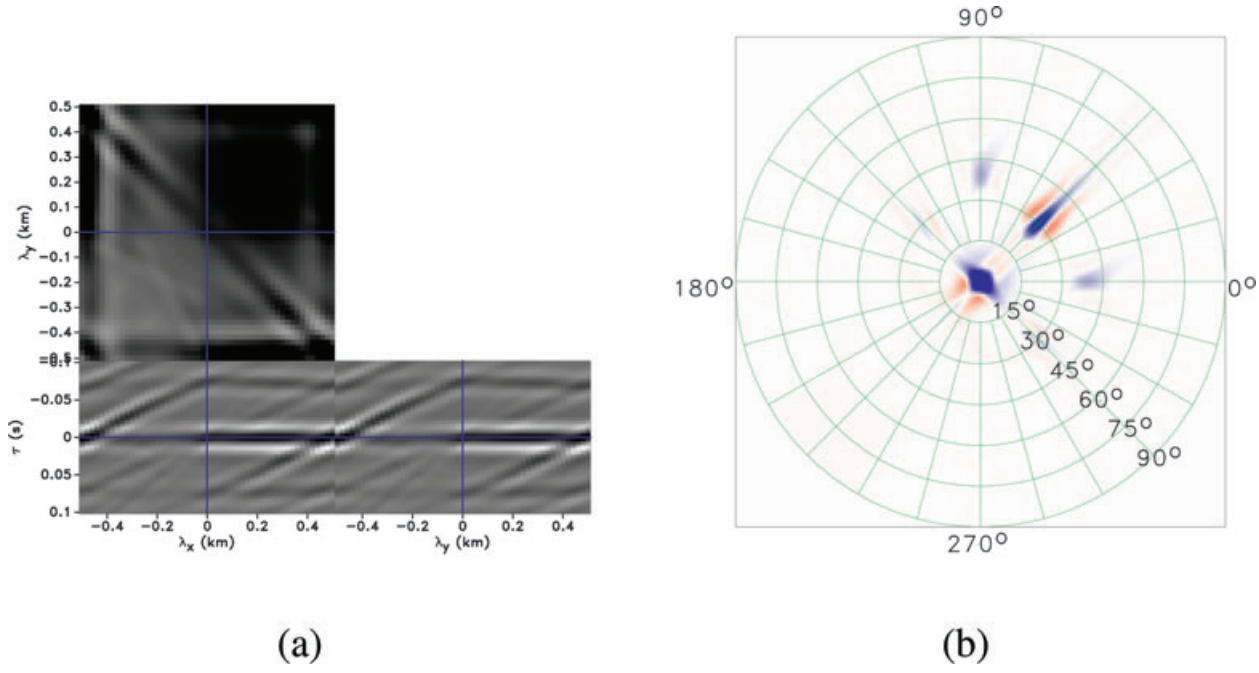


Figure 11. (a) Extended CIP and (b) wide-azimuth angle gather at coordinates $\{x = 1\,\text{km}, y = 1\,\text{km}, z = 1.2\,\text{km}\}$ for the model with reflections from multiple directions shown in Figure 9-10(b).

imaging condition is applicable equally well when migration is done with downward continuation or time reversal, or whether the model used for wavefield reconstruction is isotropic or anisotropic.

The angle decomposition can separate the precise reflection angles (aperture and azimuth), regardless of the complexity of wave propagation in the overburden and the heterogeneity of the model parameters. In particular, our technique does not require the TI anisotropic model to align with the reflector orientation, thus giving us full flexibility to handle arbitrary TI media.

The extended common-image-point gathers encode information from all wavefield branches and all experiments used for imaging. Thus angle decomposition unravels all illumination directions equally well and at no additional computational cost over that of imaging an individual event from a given experiment. The methodology is mainly applicable to the study of illumination in the subsurface, and potentially for amplitude-versus-angle analysis.

ACKNOWLEDGMENTS

We acknowledge stimulating discussions with graduate students Bharath Shekar and Julio Frigerio. The reproducible numeric examples in this paper use the Madagascar open-source software package freely available from http://www.reproducibility.org.

REFERENCES

Alkhalifah T. 2000. An acoustic wave equation for anisotropic media. *Geophysics* **65**, 1239–1250.

Alkhalifah T. and Fomel S. 2010. Angle gathers in wave-equation imaging for transversely isotropic media. *Geophysical Prospecting*, published online.

Alkhalifah T. and Sava P. 2010. A transversely isotropic medium with a tilted symmetry axis normal to the reflector. *Geophysics (Letters)* **75**, A19–A24.

Baysal E., Kosloff D.D. and Sherwood J.W.C. 1983. Reverse time migration. *Geophysics* **48**, 1514–1524.

Berkhout A.J. 1982. *Imaging of acoustic energy by wave field extrapolation*. Elsevier.

Biondi B. and Symes W. 2004. Angle-domain common-image gathers for migration velocity analysis by wavefield-continuation imaging. *Geophysics* **69**, 1283–1298.

Biondi B. and Tisserant T. 2004. 3D angle-domain common-image gathers for migration velocity analysis. *Geophys. Prosp.* **52**, 575–591.

Brandsberg-Dahl S., de Hoop M.V. and Ursin B. 2003. Focusing in dip and AvA compensation on scattering-angle/azimuth common image gathers. *Geophysics* **68**, 232–254.

Clærbout J.F. 1985. *Imaging the Earth's interior*. Blackwell Scientific Publications.

Clarke R., Xia G., Kabir N., Sirgue L. and Michell S. 2006. Case study: A large 3D wide azimuth ocean bottom node survey in deepwater gom. *SEG Technical Program Expanded Abstracts* **25**, 1128–1132.

Cullison T. and Sava P. 2011. An image-guided method for automatically picking common-image-point gathers. Presented at the 81st Annual International Meeting, SEG, Expanded abstracts.

de Bruin C.G.M., Wapenaar C.P.A. and Berkhout A.J. 1990. Angle-dependent reflectivity by means of prestack migration. *Geophysics* **55**, 1223–1234.

Duveneck E. and Bakker P.M. 2011. Stable p-wave modeling for reverse-time migration in tilted ti media. *Geophysics* **76**, S65–S75.

Fletcher R.P., Du X. and Fowler P.J. 2009. Reverse time migration in tilted transversely isotropic (TTI) media. *Geophysics* **74**, WCA179–WCA187.

Fowler P.J., Du X. and Fletcher R.P. 2010. Coupled equations for reverse time migration in transversely isotropic media. *Geophysics* **75**, S11–S22.

Gray S.H., Etgen J., Dellinger J. and Whitmore D. 2001. Seismic migration problems and solutions. *Geophysics* **66**, 1622–1640.

Koren Z., Ravve I., Ragoza E., Bartana A., Geophysical P. and Kosloff D. 2008. Full-azimuth angle domain imaging. *SEG Technical Program Expanded Abstracts* **27**, 2221–2225.

McMechan G.A. 1983. Migration by extrapolation of time-dependent boundary values. *Geophys. Prosp.* **31**, 413–420.

Michell S., Shoshitaishvili E., Chergotis D., Sharp J. and Etgen J. 2006. Wide azimuth streamer imaging of mad dog; have we solved the subsalt imaging problem? *SEG Technical Program Expanded Abstracts* **25**, 2905–2909.

Regone C. 2006. Using 3D finite-difference modeling to design wide azimuth surveys for improved subsalt imaging. *SEG Technical Program Expanded Abstracts* **25**, 2896–2900.

Rickett J. and Sava P. 2002. Offset and angle-domain common image-point gathers for shot-profile migration. *Geophysics* **67**, 883–889.

Sava P. and Fomel S. 2003. Angle-domain common image gathers by wavefield continuation methods. *Geophysics* **68**, 1065–1074.

Sava P. and Fomel S. 2005. Coordinate-independent angle-gathers for wave equation migration. 75th Annual International Meeting, SEG, Expanded Abstracts, 2052–2055.

Sava P. and Fomel S. 2006. Time-shift imaging condition in seismic migration. *Geophysics* **71**, S209–S217.

Sava P. and Vasconcelos I. 2011. Extended imaging condition for wave-equation migration. *Geophysical Prospecting* **59**, 35–55.

Sava P. and Vlad I. 2011. Wide azimuth angle gathers for wave-equation migration. *Geophysics* **76**, S131–S141.

Thomsen L. 2001. Seismic anisotropy. *Geophysics* **66**, 40–41.

Tsvankin I. 2005. *Seismic signatures and analysis of reflection data in anisotropic media*. Elsevier.

Wu R.-S. and Chen L. 2006. Directional illumination analysis using beamlet decomposition and propagation. *Geophysics* **71**, S147–S159.

Xie X. and Wu R. 2002. Extracting angle domain information from migrated wavefield. 72nd Ann. Internat. *Mtg, Soc. of Expl. Geophys.*, 1360–1363.

Xu S., Chauris H., Lambare G. and Noble M.S. 1998. Common angle image gather: A new strategy for imaging complex media. 68th Ann. Internat. *Mtg, Soc. of Expl. Geophys.*, 1538–1541.

Xu S., Zhang Y. and Tang B. 2010. 3D common image gathers from reverse time migration. *SEG Technical Program Expanded Abstracts* **29**, 3257–3262.

Zhang Y., Zhang H. and Zhang G. 2011. A stable tti reverse time migration and its implementation. *Geophysics* **76**, WA3–WA11.

Zhu X. and Wu R.-S. 2010. Imaging diffraction points using the local image matrices generated in prestack migration. *Geophysics* **75**, S1–S9.